ACS OMEGA

Open Access

This article is licensed under CC-BY-NC-ND 4.0

http://pubs.acs.org/journal/acsodf

Article

Polymorphism in oxyresveratrol studied by 3D ED

Elena Husanu, Vincentia Emerson Agbemeh, Iryna Andrusenko, Danilo Marchetti, Daniele Sonaglioni, and Mauro Gemmi*

Cite This: *ACS Omega* 2024, 9, 41555−41564

Read Online

ACCESS | Metrics & More | Article Recommendations | Supporting Information

ABSTRACT: The polymorphism of oxyresveratrol, a natural extract widely used in traditional Asian medicine, was investigated by means of the most recent structure characterization techniques. A previously unknown anhydrate oxyresveratrol crystal structure was identified for the first time from a submicrometric polyphasic mixture using 3D electron diffraction (3D ED). Additionally, a new polymorph of the dihydrate form of oxyresveratrol was also discovered and structurally studied. Detailed thermal and calorimetry studies revealed their thermal behavior and dehydration path. DFT calculations were also employed to investigate the stability of the rotational conformers involved in the hydrated phases (in both new and already known phases). This research exemplifies how 3D ED combined with cryo-plunging and routine solid-state analysis can elucidate the polymorphism scenario of a nanocrystalline natural compound.

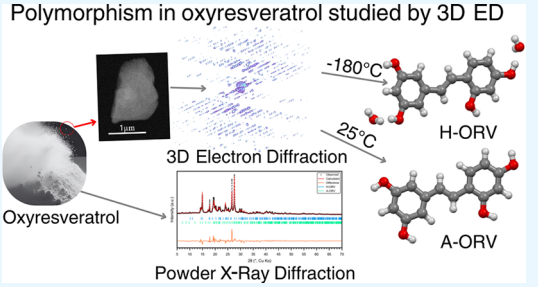

INTRODUCTION

Polymorphism refers to a substance's ability to manifest in multiple crystalline structures, each with distinct molecular arrangements and conformations within the crystal lattice.[1] The polymorphism phenomenon is known from 1832 and the first organic compound, benzamide, was reported by Liebig and Wohler.[2] However, the crystal structure of stable benzamide form was reported after more than 100 years in 1959 while the crystal structures of the unstable and originally metastable forms were reported in 2005 and 2007.[1] The time required for solving the crystal structure of organic compounds, together with the difficulty of growing good single crystals, made this research area understudied for the great part of 20th century.[1] In pharmaceutical industries, polymorph screening holds significant importance because different molecular packings within the crystal lattice result in unique physical and pharmaceutical attributes.[3] Consequently, the regulation of polymorphism poses a perennial challenge.[4] A revival of the field started in the early 90s mostly related to patent litigation.[5] The pharmaceutical industry is interested in patenting different polymorphs of active pharmaceutical compounds gaining in this way the monopole in the production of a certain drug and as a consequence, delaying the production of generic drugs by other companies.[5] Particularly noteworthy is the pharmaceutical industry's encounter with a prominent polymorphism instance concerning Ritonavir, an HIV therapeutic agent, where its transformation from form I to form II had considerable economic repercussions, culminating in its market discontinuation.[6] An exhaustive exploration into the polymorphic terrain of Ranitidine resulted in the extension of its pre-existing patent by incorporating a form II variant exhibiting analogous antiulcer properties.[6] Through this strategic maneuver, the company experienced a substantial surge in its profitability.

In active pharmaceutical compounds, polymorphism is a quite common feature more than 74% of them exhibit it.[7] To underline the interest of the pharmaceutical industry in this area, we also mention some examples of polymorphisms that have been found for some well-known drugs. Paracetamol has nine polymorphs, six at ambient pressure,[8−10] two at low pressure,[11] and one at low temperature.[12] Aspirin was believed until recently to have only three polymorphs, one that is unstable at ambient pressure, but in 2017, another polymorph was discovered stable at ambient conditions.[13] Carbamazepine presents five anhydrous polymorphs the most stable is form III and the last stable is form II.[14] Sulfathiazole presents five anhydrous polymorphs and hundreds of solvates.[3] However, the rich polymorphism of active compounds is not always reported due to the difficulties in growing crystals suitable for being characterized with conventional X-ray analysis.[3]

Natural compounds have been used since ancient times for the healing of different diseases. They are biologically active phytonutrients or phytochemicals that are present in plants with enormous health properties.[15] Traditional medicine forms the foundation of widely used drugs such as aspirin, as well as vinblastine and vincristine, vital components in childhood cancer treatment.[16] Moreover, the World Health Organiza-

Received: June 5, 2024
Revised: August 16, 2024
Accepted: August 20, 2024
Published: September 24, 2024

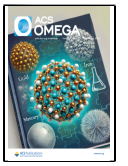

© 2024 The Authors. Published by American Chemical Society

tion's 2019 report revealed that over 40% of contemporary pharmaceutical products either originate from natural compounds or draw inspiration from traditional sources in their structural design.[17] The efforts of scientists inspired by traditional medicine to cure important diseases like malaria, were recognized by awarding the Nobel Prize for medicine to two groups that discovered the activity of avermectin and artemisinin.[18] Natural compounds can be classified from chemical structure as terpenoids, carotenoids, phenolic acids, stilbenes, coumarins, tannins, etc.[19] Polymorphism is also a central topic in natural compounds: model cases are quercitine and curcumin. Quercitine is an intensively studied natural compound that is widely used in the nutraceuticals and food industry.[20] Its interest arises from its health benefits, such as antioxidant, anti-inflammatory, and antitumoral properties.[21] Its polymorphism reveals two anhydrous polymorphs and several solvates.[20] Curcumin, which is known to have anti-HIV and antimicrobial properties, exhibits a complex polymorphism with three anhydrous polymorphs discovered up to now.[22]

Among stilbenes, trans-resveratrol stands out owing to its pharmacological potential including antidiabetic, cardioprotective, neuroprotective, and anticancer properties, which allowed its entrance on the market as a dietary supplement.[23,24] From a chemical point of view, it is a compound formed by two phenyl rings linked by an olefinic bond. One of the two aromatic rings contains two hydroxyl groups, and the other contains only one hydroxyl group. Another analogous compound with properties akin to those of trans-resveratrol, namely, oxyresveratrol, has been utilized for centuries in traditional Asian medicine. Specifically, oxyresveratrol (ORV), known as (trans-2,3′,4,5′tetrahydroxystilbene), is found in various plant sources and is notably abundant in Morus alba cultures and occurs in smaller quantities in *Artocarpus lakoocha* Roxburgh.[25,26] Comparable to trans-resveratrol, oxyresveratrol possesses a molecular structure comprising two phenyl rings linked by an olefinic bond (Figure 1). However, differently from resveratrol,

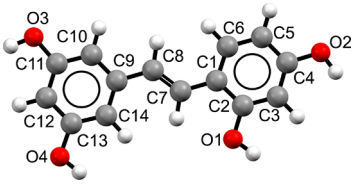

Figure 1. Molecular structure of oxyresveratrol (ORV). The structure is shown with the atomic labeling adopted in the paper.

it has both aromatic rings adorned with two hydroxyl groups. In traditional Chinese and Thai medicine, oxyresveratrol is renowned for its multifaceted therapeutic properties, anti-inflammatory, antiviral, antifungal, neuroprotective, and anticancerous activity.[25−28] Furthermore, it was also tested for its antibrowning capacity in the food industry more precisely in the clouding apple juice.[29] However, despite its various pharmaceutical properties, any step in advancing the manufacturing process necessitates a thorough comprehension of its solid-form landscape.

A close look in the Cambridge Crystallographic Data Center (CCDC) revealed that oxyresveratrol appeared to be known in only one hydrate form and two cocrystals.[30,31] This limitation could be due to the combined difficulty of the extraction of natural products and their subsequent crystallization in large crystals suitable for structure determination with the single-crystal X-ray diffraction (SCXRD) technique. Although powder X-ray diffraction (PXRD) can be a possible solution to address this obstacle, its use for natural products, which may be polyphasic, can be extremely challenging.[15]

In recent years, a new technique has emerged, 3D electron diffraction (3D ED), which can provide single crystal diffraction data suitable for structure analysis on crystal grains that are a few hundred nanometers in size and can be a breakthrough for the problem of polymorphism in pharmaceutical compounds both synthetic and natural. 3D ED is usually performed on a transmission electron microscope (TEM) and very recently, dedicated electron diffractometers have also been developed.[32,33] 3D ED has been demonstrated to be successful in the structure determination of organic compounds of pharmaceutical interests (a review can be found in ref[34]) and has elucidated long-lasting problems in pharmaceutical polymorphism for example on orthocetamol,[35] indomethacin,[36] and olanzapine.[37] Recently its application has been proposed for the structure determination of natural products[38] with the first new structures that start to be published.[39]

In this paper, we report how, thanks to the use of 3D ED, we discovered the first anhydrous form of ORV (A-ORV) and another, previously never observed, hydrate polymorph (H-ORV). The existence of anhydrate and dihydrate solid forms was confirmed by PXRD and DSC analysis. Moreover, DFT calculations were performed to investigate the stability of the two observed molecular conformations of the ORV. A thorough characterization of the solid-state polymorphism of this natural compound could offer valuable insights into the rational design of new solid forms of drugs with improved efficacy, safety, and other desirable properties.

RESULTS AND DISCUSSION

Anhydrate ORV Phase. Even though there is a plethora of applications, very little is known about the crystal structure of ORV. In the CSD database, only a hydrated structure can be found (ref code: ZAPDOL), for this reason, when we purchased an anhydrous batch of oxyresveratrol for cocrystallization studies, we performed a preliminary PXRD analysis to verify its crystalline state. Remarkably the pattern obtained could not be indexed with the structure of the only reported hydrate phase (see Figure S1a).[30] Since all attempts to crystallize the ORV in its pure phase by isolating single crystals large enough for SCXRD analysis failed, 3D ED was employed in the structural characterization of the as-received sample. Several individual thin plate-like nanocrystals were easily detected in the TEM (see inset in Figure 2), and more than 10 3D ED data acquisitions were collected on them. All 3D ED data could be indexed with a pseudo-orthorhombic primitive unit cell with approximate parameters a = 5.05(1) Å, b = 12.7 (1) Å, c = 18.1(1) Å and one of the angles slightly off from 90°, 91.4 (1)°. The observed extinctions (Figure 2 and Figure S8) point convincingly to the presence of a c glide plane. After several trials in orthorhombic and monoclinic space groups (see Experimental Section), the structure could be successfully solved *ab initio* in the monoclinic space group *Pc* (7) and all non-hydrogen atoms (36 in the asymmetric unit) were detected. The structure is a new anhydrous ORV polymorph (A-ORV).

To improve the accuracy, the structure was dynamically refined against $|F|$.[2] More details about the structure

https://doi.org/10.1021/acsomega.4c05292
ACS Omega 2024, 9, 41555−41564

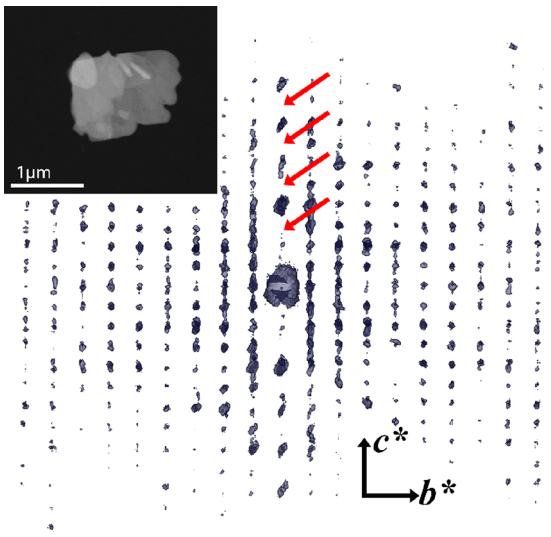

Figure 2. Reconstruction of the reciprocal space of A-ORV view along the a^* reciprocal direction. The arrows highlight the extinctions corresponding to the reflection condition $h0l$:$l = 2n$ characteristic to a c glide plane perpendicular to b. In the box at the top left is displayed a HAADF-STEM image of typical crystals of A-ORV used for 3D ED data collection.

determination and refinement from 3D ED data are reported in Table S1.

In the structure of A-ORV (Figure 3) the molecules are arranged in layers of chains stacked along the b axis. Each layer is formed by just one of the two independent molecules of the asymmetric unit, and the chains in it run parallel either to [401] or [-401] directions, depending on which molecule belongs to the layer. The layers alternate in the stacking as can be seen by the staggered configuration of the molecules when viewed along b. The molecules are disposed in a head-to-tail fashion along the chains and are held in place by H bonds involving the OH groups that are present in the *para* and *para′* position of the aromatic ring and the OH situated in the *meta* position of the other ring. Only one H bond is between two consecutive molecules of the same chain (O3−H3A···O4), while all the others are laterally connecting adjacent layers, while the chains in the same layers interact with each other through $\pi-\pi$ interactions.

Interestingly, the calculated PXRD pattern from this new A-ORV polymorph does not match completely the pattern collected on the as-received sample, as can be observed in Figure S1b. Its most intense peaks can be retrieved in the pattern, but others cannot be fitted. This suggests that the sample could be a mixture of more phases, probably with water inside, and that under the TEM vacuum conditions, one or more of these phases undergo a phase transition.

Thermal Stability Investigations. To investigate the presence of hydrated phases in the sample, we proceeded with thermogravimetric (TGA) and DSC analyses. Interestingly, by observing the TGA curve a mass loss of 5.5% in the interval 298−393 K was registered (Figure S2). In the DSC curve in the same range of 350−383 K one endothermic peak with the maximum registered at 367 K could be attributed, for its asymmetric shape, to the superposition of two phenomena: the evaporation of the absorbed water (at lower temperature) together with the loss of the bound water (Figure S2). Between 457 and 487 K, it could be observed that one endothermic peak merged with an exothermic peak associated with the melting and the onset of the decomposition of the compound, respectively. In order to understand how the sample is modified by losing water, *in situ* variable temperature PXRD (VT-PXRD) was performed from room temperature up to 390 K, which is the range where the water is lost according to the TGA profile (Figure S3). Surprisingly, the sample was stable until 370 K, the pattern remaining unchanged, but in the range of 370−390 K, some of the peaks were losing their intensity, while others remained unchanged. The final pattern at 403 K could be indexed as pure A-ORV suggesting, together with TGA/DSC, that the sample underwent dehydration and that two or more structures could be present in the original sample.

The structure of A-ORV can be isolated in any desired quantity as a pure phase by maintaining the as-received ORV at 403 K in reduced pressure overnight. The PXRD of this final product could be indexed with the 3D ED A-ORV primitive monoclinic cell, which could be refined with a Le Bail fit to a = 4.9417(6) Å, b = 12.4553(15) Å, c = 18.1194(18) Å, β = 89.9094(18) °, V = 1115.3(2) Å^3 (Figure S6). A Rietveld refinement was conducted using the 3D ED structure as the starting model, achieving convergence at R_p = 8.20% and wR_p = 12.45% (Figure S7). The resulting structural model from the Rietveld refinement exhibits an identical molecular configuration to the initial 3D ED model, highlighting the accuracy of this latest technique. Some of the peaks in the refinement could not be optimally fitted both in intensity and profile shape. This may potentially be associated with phenomena that

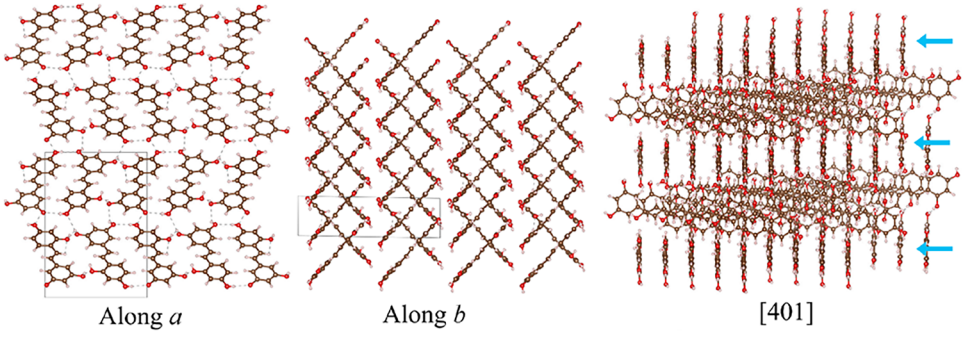

Figure 3. Crystal structure of A-ORV view along *a, b* axes and along [401] direction. In the view along b, the staggered configuration of the two chain systems is clearly visible. If the structure is viewed along [401] the interpenetration of the two chain systems can be seen. In the figure three chain layers running along [401] are displayed (indicated by light blue arrows) alternated with two layers of chains running along [−401]. Color code: brown C, red O, white H.

https://doi.org/10.1021/acsomega.4c05292
ACS Omega 2024, 9, 41555−41564

are challenging to assess, such as minor H-ORV contamination, positional disorder, and anisotropic particle strain. A careful inspection of the experimental PXRD pattern of the as-received ORV reveals that several peaks can be fitted by the A-ORV simulated pattern, indicating that A-ORV is already present in the as-received sample (Figure S10).

The thermal properties of A-ORV, as a pure phase, were investigated by DSC. The A-ORV sample showed a similar behavior to the as-received sample, and the only difference is that the endothermic peaks corresponding to water loss were no longer present (Figure S4a). If the thermal analysis is pushed beyond the melting, there is evidence of degradation (Figure S4a), which happens already during the melting process as confirmed by the shifting in the glass transition of the just melted sample during consecutive heating scans (Figure S4b and discussion in the Supporting Information). As a final consideration, it is of interest to note that for A-ORV, the ratio between the glass transition temperature and the melting temperature is around 0.8: according to Tu et al.[40] Such a ratio higher than 0.7 is a good indication of a high glass forming ability, meaning that the glassy state remains stable with time without crystallization.

New Hydrated ORV Phase. To confirm the presence of H-ORV and to be able to study its properties, we tried to synthesize it as a pure phase by placing the as-received ORV in a mixed solution of $CHCl_3/CH_3OH$, as mentioned in the Experimental Section, and let it evaporate. To ensure the complete evaporation of the solvent, the solid sample was transferred in a vacuum oven at 40 °C and a PXRD pattern was collected after complete evaporation. This, if combined with the pattern of A-ORV, could account for all the peaks of the as-received sample, supporting the hypothesis of a two-phase sample. However, it is different from the simulated pattern of the only reported hydrated form (see Figure S1a,b), indicating a possible discovery of a new polymorph. Since no crystalline hydrated phase was ever observed inside TEM in the original sample, but several amorphous grains were now and then detected, we deduced that the high vacuum was responsible for the dehydration of H-ORV. To avoid this phenomenon, the sample was prepared with a cryo-plunging method similar to the one used in cryo-EM (as described in the Experimental Section). The cryoprotection given by the amorphous ice successfully preserved the hydrated H-ORV structure. Interestingly, the morphology of H-ORV nanocrystals appeared to be very similar to the anhydrate form (Figure 4). A similar approach has also been used in the structure determination of porous materials (e.g., MOFs) to stabilize the guest H_2O molecules present in their porous structures.[41,42] 3D ED data sets were recorded on three crystal fragments, and all were consistent with a primitive monoclinic cell with approximate parameters of a = 8.87 (1) Å, b = 8.11(1) Å, and c = 9.29(1) Å with a beta angle of 90.9(1)°. Upon inspection of the reciprocal space reconstruction, the reflection conditions $h0l$:l = 2n were identified (Figure 4 and Figure S12), suggesting the presence of a c glide plane perpendicular to b. The structure of H-ORV was then solved *ab initio* by direct methods in space group *Pc* (7) and later refined by using kinematical refinement with isotropic thermal factors. The structure turned out to be dihydrated with two water molecules in the asymmetric unit (Figure S13).

More details about structure determination and refinement from 3D ED data are reported in Table S1 and in the Experimental Section. Unfortunately, the quality of the 3D ED data collected on H-ORV is not high enough for dynamical refinement and for the determination of the hydrogen positions; therefore, in this case, the network of the hydrogen bonding can only be guessed.

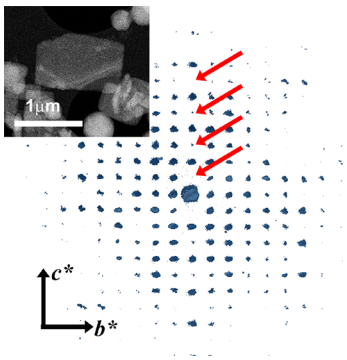

Figure 4. Reconstruction of the reciprocal space of H-ORV view along the a* reciprocal direction. The arrows highlight the extinctions corresponding to reflection condition $h0l$:l = 2n. In the box at the top left is displayed a HAADF-STEM image of typical crystals of H-ORV used for 3D ED data collection.

Again, the choice of a primitive monoclinic unit cell was supported by the successful indexing and Le Bail fitting of the PXRD pattern, from which we obtained the refined lattice parameters: a = 8.7224(3) Å, b = 8.0157(4) Å, c = 9.3326(3) Å, β = 91.3848(17)°, and V = 652.31(5) (Figure S11).

Furthermore, the 3D ED structural model of H-ORV was refined against the PXRD data using the Rietveld approach. The ORV molecule was refined as a semirigid body, in which the aryl group was left free to rotate around their related single bonds. Then, the positions of the solvent-related oxygen atoms were left free to refine without any restraint. The refinement converged to R_p = 8.02% and wR_p = 11.68% (Figure 5). The resulting structural model is in agreement with the 3D ED model.

In H-ORV the ORV molecules form planes parallel to (10−1). Inside each plane, the molecules are arranged in a head-to-tail fashion, like in A-ORV, forming chains (Figure 6 and Figure S13). The bonding between the molecules along the chain and within the chains is guaranteed by the water molecules through a network of hydrogen bonds. Each water molecule, in fact, has a distorted tetrahedral contact geometry with four other oxygens of ORV molecules, three with molecules within the layer and one with a molecule of another layer (above or below), possibly forming four hydrogen bonds (Figure S14). In adjacent planes, the chains run along two different directions, [111] and [1−11] forming an angle close to 65°. It is very interesting to compare the packing of H-ORV with ZAPDOL (Figure S15). Both the ZAPDOL and H-ORV contained two molecules of water, but ZAPDOL crystallizes in the triclinic centrosymmetric space group *P-1*.[30] Also, in ZAPDOL the ORV molecules are packed in planes of head-to-tail ORV molecules chains, but, due to the presence of the center of symmetry, adjacent chains run in opposite directions. The water molecules are responsible for the bonding along the chains, but in this case, also a direct hydrogen bonding between the water molecules is present.

Also, for the H-ORV as a single phase, thermal investigations were performed. The DSC plot showed a highly intense and broad peak in the region 350−425 K, attributable to water loss, and then a melting peak followed by an exothermic peak,[43] in a

https://doi.org/10.1021/acsomega.4c05292
ACS Omega 2024, 9, 41555−41564

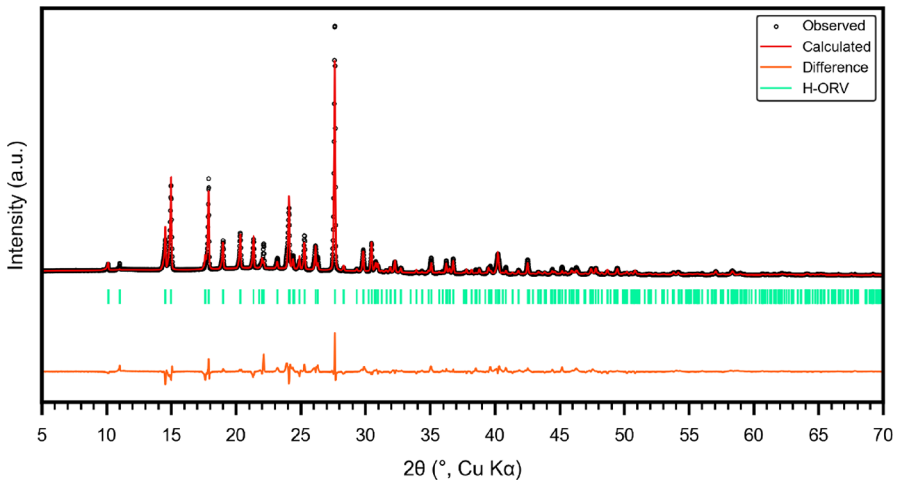

Figure 5. Profile fit from Rietveld refinement on PXRD data of H-ORV. The shown range is limited to 2θ values of 5−70° for clarity, whereas the refinement was carried out in the range 3−90°. The refinement converged to R_p = 8.02% and wR_p = 11.68%.

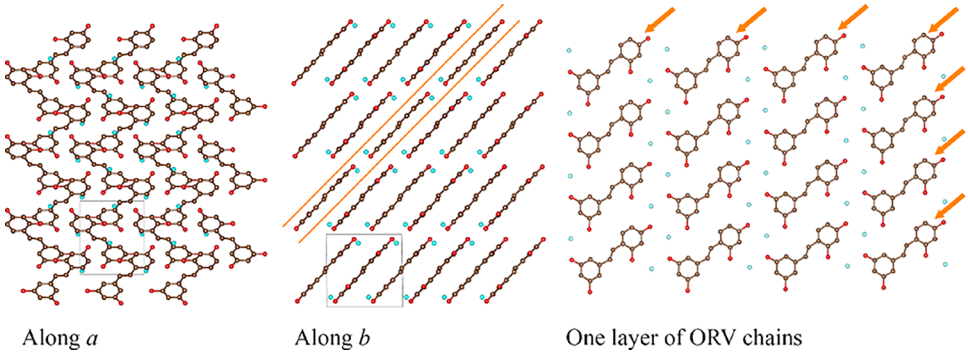

Figure 6. (Left and center) Crystal structure of H-ORV view along *a*, *b* without hydrogens. (Right) In the *b* projection, one layer of molecule chains is highlighted by orange lines. The chains are indicated by orange arrows. Color code: brown C, red O, light blue O of the water molecules.

similar fashion to what happens to the as-received ORV (Figure S5). The absence of a glass transition, unless melting is reached, testifies that after water loss the sample remains crystalline (inset of Figure S5), confirming the formation of the anhydrate form. This result is consistent with a direct transformation to the anhydrous crystalline phase after the loss of the water molecules embedded in the crystalline network.[44] Our findings are in agreement with other studies made on active pharmaceutical compounds like naproxen sodium[44] or baclofen[45] that have the same behavior: after water loss the compounds they are transformed directly in anhydrous crystalline phases. Worthily to mention is that in the DSC curve, we did not observe any other peaks that might be attributed to the amorphization or the formation of other crystalline forms. The melting process was in concomitance with the starting of the degradation of the sample.

Finally, to confirm that the as-received sample was a mixture of both phases, we performed a Rietveld refinement of its PXRD as a mixture of H-ORV and A-ORV. The Rietveld refinement successfully converged to a composition of 58.9% A-ORV and 41.1% H-ORV (Figure S16). Using this estimate for the composition of the mixture and considering that the H-ORV is dihydrated, we can estimate the maximum weight loss in case of full dehydration of H-ORV which is 5.6%, in well agreement with the 5.5% weight loss measured by TGA.

A peculiarity of the H-ORV structure lies in the different conformations of the embedded ORV molecules, in which one of the two aryl rings is rotated 180° around the C1−C7 bond (Figure 1) compared to the A-ORV and ZAPDOL structures (Figure 7a). For the sake of clarity, we have labeled the ORV conformations as form 1 for the conformer of the A-ORV structure, and form 2 for the H-ORV conformer. Molecular modeling studies, conducted considering a single molecule in vacuum, revealed a stabilization energy of 1.94 kJ mol^{-1} for form 1 with respect to form 2, leading at room temperature to a species distribution of ∼2:1. The activation energy of the aryl group rotation (22.72 kJ mol^{-1}) results to be slightly higher than the energy required for a rotation of the single C−C bond in a vinylbenzene-like system (usually ∼10 kJ mol^{-1}).[46] This makes the rotation the rate-determining step of the interconversion process (Figure 7). However, the solid-state interactions in H-ORV are enough to stabilize the ORV molecule in form 2. Furthermore, if the crystallization is performed at room temperature the product results are composed of a small amount of ZAPDOL phase (4.6% v/v), which contains the ORV form 1 (Figure S17). Indeed, the concomitance appearing of two or more polymorphs is a known phenomenon in the crystallization process.[37,47] When the system was heated at 40 °C under reduced pressure, the ZAPDOL phase disappeared and led to the pure phase of H-ORV.

Similar features were observed also for other compounds like diphenyl carbamide which crystallizes in three forms α, β, and γ. Form α crystallizes concomitantly with form β in the range

https://doi.org/10.1021/acsomega.4c05292
ACS Omega 2024, 9, 41555−41564

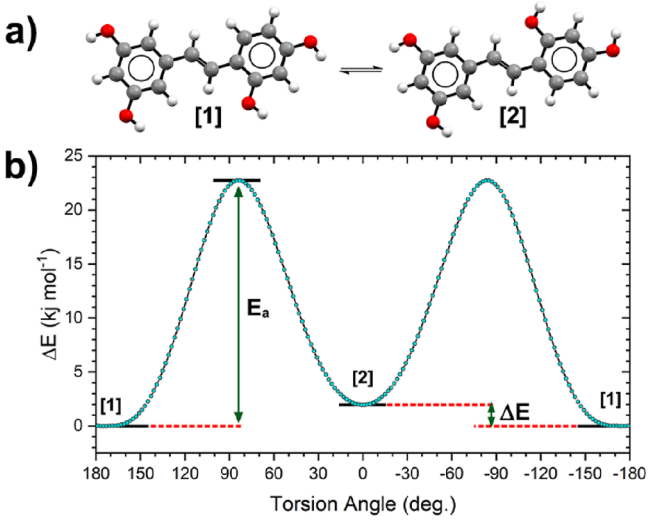

Figure 7. (a) Interconversion equilibrium between ORV forms 1 and 2. The related thermodynamic equilibrium constant is $K = 0.46$. (b) The plot represents the molecular energy as a function of the dihedral angle involved in the interconversion equilibrium. $\Delta E = 1.94$ kJ mol^{-1} and $E_a = 22.72$ kJ mol^{-1}. The calculations were conducted by using a DFT theory level with a B3LYP functional and a 6-311+(3d, p) basis set.

of temperatures between 35 and 75 °C. The relative amounts can be controlled by variation of temperature; at high temperatures, the majority of the α form is registered. At 13 °C, the γ form appears, and small amounts of β form with increasing temperature. However, at 40 °C the γ form disappears completely, and small amounts of α form appear,[47] a similar behavior to our system where heating at 40 °C under reduced pressure leads to a full conversion of the ZAPDOL phase into H-ORV.

CONCLUSIONS

This work is an example of how 3D ED can increase our knowledge of the crystal chemistry of natural compounds that although widely used in medicine or the food industry, like oxyresveratrol, are very poorly characterized from the crystallochemical point of view. In the case of oxyresveratrol, the sample purchased from a chemical dealer already exhibited new crystal forms never reported before. Thanks to 3D ED, both of these forms were detected and solved. One is the first anhydrous oxyresveratrol form ever observed. The second is a new dihydrated polymorph, which has been quite hard to study inside the TEM because of its high sensitivity to vacuum. To avoid its dehydration inside the microscope, we had to adapt a specific cryo-plunging sample preparation procedure, which succeeded in cryoprotecting the new hydrated phase which successfully remained crystalline inside TEM. Once detected, the two new structures have been synthesized as pure phases and their PXRD patterns fully fitted with a Rietveld refinement procedure, confirming with another radiation their correct structure. Both phases were thermally characterized, and also the presence of a new distorted form of oxyresveratrol molecule was justified through DFT calculations. We can state that the workflow of our study can be considered as a model to apply to the structure characterization to many other natural compounds, and we expect that this will produce the discovery of many new polymorphs.

EXPERIMENTAL SECTION

Oxyresveratrol, methanol, and chloroform (all from Sigma-Aldrich) were used as-received for the crystallization of the ORV hydrated form. The oxyresveratrol was a batch with Mw = 244.02 g mol^{-1} (anhydrate compound).

Preparation of A-ORV. The anhydrous ORV was prepared by introducing the as-received sample of ORV in a vacuum furnace at 130 °C until the disappearance of the characteristic peaks attributed to the hydrated form in the PXRD pattern.

Preparation of H-ORV. The received ORV was placed in a beaker and dissolved in $CHCl_3$/MeOH (4/1v/v). A yellow liquid was formed and filtered. After the beaker was covered with parafilm, small holes were made on it and let slowly evaporate under the hood. To be sure that the solvent evaporated completely, the sample was later left at 40 °C in a vacuum Buchi oven.

General Procedures. *Microscopy and 3D Electron Diffraction (3D ED).* High-angle annular dark-field scanning transmission electron microscopy (HAADF-STEM) imaging and ED data were recorded with Zeiss Libra 120 transmission electron microscope (TEM) operating at 120 kV and equipped with a LaB_6 source. 3D ED data collections were performed in both continuous rotation (cRED) and precession-assisted stepwise (PEDT) modes.[48]

In cRED, the crystals were searched in TEM mode, and the 3D ED data were collected in nanodiffraction mode with a parallel beam of 600 nm obtained with a 19 μm C2 aperture. The crystal was tracked during rotation with an in-house developed tracking which allows for a full data collection in about 170 s, drastically reducing the total dose to around 1 el Å^{-2}. cRED was used for the data collection on A-ORV.

In PEDT, the crystal search and the 3D ED experiment were performed by keeping the instrument in STEM mode. For collecting 3D ED data, the beam is defocused to have a parallel illumination on the sample, as described in ref 48. In this configuration, the electron beam size is about 150−200 nm in diameter, obtained by using a 5 μm C2 condenser aperture. The sample was rotated in fixed steps of 1°. After each tilt, a diffraction pattern was acquired with a beam precession of 1° (performed using Nanomegas Digistar P1000 device).[49] In this case, the crystal position was tracked by defocused STEM imaging at high magnification as described by Yang et al.[50]

Thanks to the very low instantaneous dose of 0.01 el Å^{-2}s^{-1}, no evidence of beam damage, indicated by fading of high-resolution reflections or appearance of amorphous rings, was ever observed even in stepwise mode, which requires a higher total exposure time per experiment.[48] The 3D ED data sets covered range from 90 to 110°. A camera length of 180 mm was used, allowing for a resolution in real space of about 0.7 Å. All 3D ED data were recorded using the single-electron ASI TIMEPIX detector.[51]

3D ED experiments were carried out both at room temperature and at −180 °C, for the structure solution of the anhydrous phase and for obtaining the structure of the dihydrated phase, respectively. For the room temperature experiment, the sample preparation involved gently crushing a small amount of powder between two glass slides and directly loading it onto a carbon-coated Cu TEM grid without any solvent or sonication. For the cooling experiment, the grids (Cu grids coated with quantifoil R 2/1 holey films with regular circular holes of 2 μm in diameter) were treated with an oxygen plasma cleaner for 30 s at 20 W and used within 1 h to

https://doi.org/10.1021/acsomega.4c05292
ACS Omega 2024, 9, 41555−41564

maintain stable hydrophilicity of the surface. A sample suspension with water was made and sonicated for about 2 min to ensure the homogeneity of the suspension and prevent agglomeration. A drop was then deposited onto the grid and the excess liquid was blotted with filter paper to ensure a thin layer of liquid on the grid (a usual cryo-plunge freezing protocol).[52] The grid was then manually picked using a tweeze and cryo-plunged into liquid ethane. Plunged grids were stored in grid boxes in liquid nitrogen and then quickly moved to the transfer station for loading into the cryotransfer holder (Gatan 626). Due to the higher mechanical instability of the cryo-holder, the data collection on H-ORV was performed in PEDT.

3D ED data were analyzed using the software *PETS2.0*[53] for unit cell determination and integration of intensities. *Ab initio* structure determination was obtained by standard direct methods (SDMs) as implemented in the software *SIR2014*[54] considering I_{hkl} intensities proportional to $|F_{hkl}|^2$ (kinematical approximation). Kinematical least-squares structure refinements were performed on the hydrate oxyresveratrol with the software *SHELXL*.[55] Due to the low-quality data, it was not possible to perform dynamical refinement in this case. For the anhydrate structure, dynamical refinement against $|F|^2$ was run using the software DYNGO embedded in the *JANA2020*[56] system. In dynamical refinement, the dynamical scattering which is unavoidable in electron diffraction is modeled through full Bloch wave calculation.[57] Only the best data set for each sample was used for the final structure refinement based on the high tilt range, highest resolution, and the absence of high background noise. Atomic structures were visualized by the software *VESTA*[58] and *Mercury*.[59]

Details of the Structure Solution and Refinement of A-ORV and H-ORV with 3D ED Data. All 3D ED data collected on A-ORV crystals could be indexed with a pseudo-orthorhombic primitive unit cell with approximate parameters a = 5.05(1) Å, b = 12.7 (1) Å, and c = 18.1(1) Å and one of the angles slightly off from 90°, 91.4 (1)°, but still compatible with orthorhombic symmetry for the precision available in our TEM in the case of critical data sets like those recorded on beam sensitive samples. With a volume of 1163(2)Å^3, the unit cell could conveniently host four ORV molecules, in apparent agreement with the multiplicity of several orthorhombic space groups. The observed extinctions (Figure 2 and Figure S8) point convincingly to the extinction symbol $P-c-$, which is compatible with the space groups $Pmc2_1$ (26), $P2cm$ (28) or $Pmcm$ (51). Nevertheless, all attempts to solve the structure with any orthorhombic space group were unsuccessful. Therefore, the symmetry was reduced to the monoclinic space group Pc (7) that implies the presence of two independent ORV molecules in the asymmetric unit. In this way, the structure could be successfully solved.

To improve the accuracy, the structure was dynamically refined against $|F|^2$ in the following way. Initially, the refinement was performed without hydrogen atoms, and restraints were imposed on the aromatic rings, interatomic distances, angles, and the flatness of the two different aromatic rings. After the first refinement, hydrogens were added automatically and constrained using the riding model. The thermal parameters of all the other atoms were refined anisotropically (Figure S9). More details about structure determination and refinement from 3D ED data are reported in Table S1.

3D ED data collected on three crystal fragments of H-ORV, were all consistent with a primitive monoclinic cell with approximate parameters of a = 8.87 (1) Å, b = 8.11(1) Å, and c = 9.29(1) Å with a β angle of 90.9(1)° and a volume of 668(2) Å^3. Such a unit cell would conveniently host only two ORV molecules. However, considering that the ORV molecule does not have 2-fold or mirror symmetry, the cell volume is not consistent with an orthorhombic system, although all the angles were close to 90°, hence the symmetry was reduced to a monoclinic setting. Upon inspection of the reciprocal space reconstruction, the reflection conditions $h0l$: l = 2n were identified (Figure 4 and Figure S12), suggesting a crystallization in space group Pc (7) or $P2/c$ (13) with one independent ORV molecule in the asymmetric unit. The structure of H-ORV was then solved ab initio by direct methods in space group Pc (7) and later refined by using kinematical refinement with isotropic thermal factors.

Powder X-ray Diffraction (PXRD) and In Situ Temperature Experiments. PXRD data were acquired in Debye−Scherrer geometry using a STOE Stadi P equipped with Cu−$K_{\alpha 1}$ radiation (λ = 1.5406 Å), a Ge (111) Johansson monochromator from STOE & Cie and a MYTHEN2 1 K detector from Dectris. All studied samples were loaded in a borosilicate glass capillary (0.5 mm external diameter) and data were acquired in the 2θ range 3−90° (corresponding to a maximum resolution of 1.09 Å) with an interval of 0.03° between consecutive points. The only exception is the data collection on as-received ORV mixed-phase samples since the purpose was just the phase quantification, they were characterized in the 3−70° angular range (corresponding to a maximum resolution of 1.34 Å). Data were preliminarily processed with *WinXPOW* (by STOE & Cie). For the variable temperature PXRD experiments (VT-PXRD), an STOE capillary furnace was mounted, and the mixed phase was loaded in 0.5 mm quartz capillary. To increase statistics and avoid preferential orientation effects, the capillary was spun. The temperature varied from 30 to 115 °C with a heating rate of 10 K/min. The detector was kept fixed at 20° recording the 2θ range 12−32°, where the peaks of interest were situated and every 10 °C, an isotherm of 3 min was done, and after, data collection was performed.

Le Bail and Rietveld refinements from PXRD were carried out with the *JANA2020* software package.[56] The background was initially described by manually picking points and then refinement against them. For the Rietveld refinement, the profile parameters were first obtained by Le Bail fitting and then kept fixed. The Rietveld refinement of the two new ORV crystal structures (A-ORV and H-ORV) was performed starting from the lattice parameters and atomic coordinates of their respective 3D ED model. In both cases, the PXRD data were obtained from nearly pure phase samples (see the SI). The ORV molecules were refined as semirigid bodies, in which the torsion angles related to single bonds were freely refined.

Differential Scanning Calorimetry (DSC) and Thermogravimetric Analysis (TGA). Conventional calorimetric measurements have been done with a differential scanning calorimeter (DSC) PerkinElmer model 8500, equipped with Intracooler III as the refrigerating system. The samples have been loaded in a 40 μL aluminum pan, and then hermetically sealed: mass ranges between 5 and 10 mg. Temperature and enthalpy scales were calibrated with Indium. Nitrogen has been used as a purge gas with a flow rate of 20 mL/min. All

https://doi.org/10.1021/acsomega.4c05292
ACS Omega 2024, 9, 41555−41564

calorimetric measurements were carried out at 10 K/min, unless otherwise explicitly stated.

In total, three samples were considered and studied: as-received ORV and two new phases (A-ORV and H-ORV). Thermogravimetric (TGA) measurements were performed with a PerkinElmer instrument, model TGA 8000, at 10 K/min only on the as-received sample.

Molecular Modeling. The ground-state geometrical optimizations of the two ORV conformers were conducted by using a DFT theory level with a B3LYP functional and a 6-311+(3d, p) basis set. The energy scan calculation was conducted by fixing the dihedral angle of interest, increasing it by 2°, and optimizing the geometry for each step. Gaussian 16 software was used to perform the previously described procedures.[60]

■ ASSOCIATED CONTENT

Supporting Information

The Supporting Information is available free of charge at https://pubs.acs.org/doi/10.1021/acsomega.4c05292.

Powder X-ray diffractions measurements; thermal analysis; Rietveld refinements; 3D ED data analysis (PDF)

■ AUTHOR INFORMATION

Corresponding Author

Mauro Gemmi − *Electron Crystallography, Center for Material Interfaces, Istituto Italiano di Tecnologia, Pontedera 56025, Italy;* orcid.org/0000-0001-9542-3783; Email: mauro.gemmi@iit.it

Authors

Elena Husanu − *Electron Crystallography, Center for Material Interfaces, Istituto Italiano di Tecnologia, Pontedera 56025, Italy*

Vincentia Emerson Agbemeh − *Electron Crystallography, Center for Material Interfaces, Istituto Italiano di Tecnologia, Pontedera 56025, Italy; Department of Chemistry, Life Sciences and Environmental Sustainability, University of Parma, Parma 43124, Italy*

Iryna Andrusenko − *Electron Crystallography, Center for Material Interfaces, Istituto Italiano di Tecnologia, Pontedera 56025, Italy;* Present Address: Center for Instrument Sharing of the University of Pisa (CISUP), University of Pisa, Lungarno Antonio Pacinotti, 43, 56126 Pisa, Italy; orcid.org/0000-0001-9554-2969

Danilo Marchetti − *Electron Crystallography, Center for Material Interfaces, Istituto Italiano di Tecnologia, Pontedera 56025, Italy; Department of Chemistry, Life Sciences and Environmental Sustainability, University of Parma, Parma 43124, Italy*

Daniele Sonaglioni − *Electron Crystallography, Center for Material Interfaces, Istituto Italiano di Tecnologia, Pontedera 56025, Italy; Dipartimento di Fisica "E. Fermi", University of Pisa, Pisa 56127, Italy*

Complete contact information is available at: https://pubs.acs.org/10.1021/acsomega.4c05292

Notes

The authors declare no competing financial interest.

■ ACKNOWLEDGMENTS

This research was supported by the European Union's Horizon 2020 research and innovation programme under the Marie Sklodowska-Curie grant agreement no. 956099 (NanED − Electron Nanocrystallography−H2020-MSCAITN).

■ REFERENCES

(1) Cruz-Cabeza, A. J.; Bernstein, J. Conformational Polymorphism. *Chem. Rev.* **2014**, *114* (4), 2170−2191.

(2) Thakuria, R.; Thakur, T. S. 5.13 - Crystal Polymorphism in Pharmaceutical Science. In *Comprehensive Supramolecular Chemistry II*; Atwood, J. L., Ed.; Oxford: Elsevier, 2017; pp 283−309.

(3) Munroe, Á.; Rasmuson, Å. C.; Hodnett, B. K.; Croker, D. M. Relative Stabilities of the Five Polymorphs of Sulfathiazole. *Cryst. Growth Des.* **2012**, *12* (6), 2825−2835.

(4) Moondra, S.; Maheshwari, R.; Taneja, N.; Tekade, M.; Tekadle, R. K. Chapter 6 - Bulk Level Properties and Its Role in Formulation Development and Processing. In *Dosage Form Design Parameters*; Tekade, R. K., Ed.; Academic Press, 2018; pp 221−256.

(5) Tandon, R.; Tandon, N.; Thapar, R. K. Patenting of Polymorphs. *Pharmaceutical Patent Analyst*. Newlands Press Ltd March 1, 2018; pp 59−63.

(6) Cruz-Cabeza, A. J.; Feeder, N.; Davey, R. J. Open Questions in Organic Crystal Polymorphism. *Commun. Chem.* **2020**, *3* (1), 142.

(7) Thakuria, R.; Thakur, T. S. Crystal Polymorphism in Pharmaceutical Science. In *Comprehensive Supramolecular Chemistry II*; Elsevier Inc., 2017; Vol. *5*, pp 283−309.

(8) Haisa, M.; Kashino, S.; Kawai, R.; Maeda, H. The Monoclinic Form of P-Hydroxyacetanilide. *Acta Crystallogr., Sect. B: Struct. Crystallogr. Cryst. Chem.* **1976**, *32* (4), 1283−1285.

(9) Perrin, M.-A.; Neumann, M. A.; Elmaleh, H.; Zaske, L. Crystal Structure Determination of the Elusive Paracetamol Form III. *Chem. Commun.* **2009**, *22*, 3181−3183.

(10) Shtukenberg, A. G.; Tan, M.; Vogt-Maranto, L.; Chan, E. J.; Xu, W.; Yang, J.; Tuckerman, M. E.; Hu, C. T.; Kahr, B. Melt Crystallization for Paracetamol Polymorphism. *Cryst. Growth Des.* **2019**, *19* (7), 4070−4080.

(11) Smith, S. J.; Bishop, M. M.; Montgomery, J. M.; Hamilton, T. P.; Vohra, Y. K. Polymorphism in Paracetamol: Evidence of Additional Forms IV and V at High Pressure. *J. Phys. Chem. A* **2014**, *118* (31), 6068−6077.

(12) Reiss, C. A.; van Mechelen, J. B.; Goubitz, K.; Peschar, R. Reassessment of Paracetamol Orthorhombic Form III and Determination of a Novel Low-Temperature Monoclinic Form III-m from Powder Diffraction Data. *Acta Crystallogr., Sect. C: Struct. Chem.* **2018**, *74* (3), 392−399.

(13) Shtukenberg, A. G.; Hu, C. T.; Zhu, Q.; Schmidt, M. U.; Xu, W.; Tan, M.; Kahr, B. The Third Ambient Aspirin Polymorph. *Cryst. Growth Des.* **2017**, *17* (6), 3562−3566.

(14) Broadhurst, E. T.; Xu, H.; Parsons, S.; Nudelman, F. Revealing the Early Stages of Carbamazepine Crystallization by CryoTEM and 3D Electron Diffraction. *IUCrJ* **2021**, *8*, 860−866.

(15) Atanasov, A. G.; Zotchev, S. B.; Dirsch, V. M. the International Natural Product Sciences Taskforce, Supuran CT. Natural Products in Drug Discovery: Advances and Opportunities. *Nat. Rev. Drug Discovery* **2021**, *20* (3), 200−216.

(16) Cubo, E.; Goetz, C. G. Antineoplastic Chemotherapy. In *Encyclopedia of the Neurological Sciences*; Aminoff, M. J., Daroff, R. B., Eds.; Academic Press: New York, 2003; pp 231−234.

(17) World Health Organization. *Traditional medicine has a long history of contributing to conventional medicine and continues to hold promise*. https://www.who.int/News-Room/Feature-Stories/Detail/Traditional-Medicine-Has-a-Long-History-of-Contributing-to-Conventional-Medicine-and-Continues-to-Hold-Promise.

(18) Harvey, A. L.; Edrada-Ebel, R.; Quinn, R. J. The Re-Emergence of Natural Products for Drug Discovery in the Genomics Era. *Nat. Rev. Drug Discovery* **2015**, *14* (2), 111−129.

(19) Teka, T.; Zhang, L.; Ge, X.; Li, Y.; Han, L.; Yan, X. Stilbenes: Source Plants, Chemistry, Biosynthesis, Pharmacology, Application and Problems Related to Their Clinical Application-A Comprehensive Review. *Phytochemistry* **2022**, *197*, No. 113128.
(20) Klitou, P.; Parisi, E.; Bordignon, S.; Bravetti, F.; Rosbottom, I.; Dell'Aera, M.; Cuocci, C.; Chierotti, M. R.; Altomare, A.; Simone, E. Navigating the Complex Solid Form Landscape of the Quercetin Flavonoid Molecule. *Cryst. Growth Des.* **2023**, *23* (8), 6034−6045.
(21) Srinivas, K.; King, J. W.; Howard, L. R.; Monrad, J. K. Solubility and Solution Thermodynamic Properties of Quercetin and Quercetin Dihydrate in Subcritical Water. *J. Food Eng.* **2010**, *100* (2), 208−218.
(22) Prasad, R.; Gupta, K. M.; Poornachary, S. K.; Dalvi, S. V. Elucidating the Polymorphic Behavior of Curcumin during Anti-solvent Crystallization: Insights from Raman Spectroscopy and Molecular Modeling. *Cryst. Growth Des.* **2020**, *20* (9), 6008−6023.
(23) Arias, A.; Costa, C. E.; Moreira, M. T.; Feijoo, G.; Domingues, L. Resveratrol-Based Biorefinery Models for Favoring Its Inclusion along the Market Value-Added Chains: A Critical Review. *Sci. Total Environ.* **2024**, *908*, No. 168199.
(24) Zarychta, B.; Gianopoulos, C. G.; Pinkerton, A. A. Revised Structure of Trans-Resveratrol: Implications for Its Proposed Antioxidant Mechanism. *Bioorg. Med. Chem. Lett.* **2016**, *26* (5), 1416−1418.
(25) Chuanasa, T.; Phromjai, J.; Lipipun, V.; Likhitwitayawuid, K.; Suzuki, M.; Pramyothin, P.; Hattori, M.; Shiraki, K. Anti-Herpes Simplex Virus (HSV-1) Activity of Oxyresveratrol Derived from Thai Medicinal Plant: Mechanism of Action and Therapeutic Efficacy on Cutaneous HSV-1 Infection in Mice. *Antiviral Res.* **2008**, *80* (1), 62−70.
(26) Likhitwitayawuid, K. Oxyresveratrol: Sources, Productions, Biological Activities, Pharmacokinetics, and Delivery Systems. *Molecules* **2021**, *26* (14), 4212.
(27) Donini, M.; Gaglio, S. C.; Laudanna, C.; Perduca, M.; Dusi, S. Oxyresveratrol-Loaded Plga Nanoparticles Inhibit Oxygen Free Radical Production by Human Monocytes: Role in Nanoparticle Biocompatibility. *Molecules* **2021**, *26* (14), 4351.
(28) Rodsiri, R.; Benya-aphikul, H.; Teerapattarakan, N.; Wanakhachornkrai, O.; Boonlert, W.; Tansawat, R.; Wiwattanapatapee, R.; Sritularak, B.; Likhitwitayawuid, K. Neuroprotective Effect of Oxyresveratrol in Rotenone-Induced Parkinsonism Rats. *Nat. Prod Commun.* **2020**, *15* (10), No. 1934578X20966199.
(29) Li, H.; Cheng, K.-W.; Cho, C.-H.; He, Z.; Wang, M. Oxyresveratrol as an Antibrowning Agent for Cloudy Apple Juices and Fresh-Cut Apples. *J. Agric. Food Chem.* **2007**, *55* (7), 2604−2610.
(30) Deng, H.; He, X.; Xu, Y.; Hu, X. Oxyresveratrol from Mulberry as a Dihydrate. *Acta Crystallogr., Sect. E: Struct. Rep. Online* **2012**, *68* (5), o1318−o1319.
(31) Ouiyangkul, P.; Saithong, S.; Tantishaiyakul, V. Syntheses and Crystal Structures of Hydrated and Anhydrous 1:2 Cocrystals of Oxyresveratrol and Zwitterionic Proline. *Acta Crystallogr., Sect. E: Crystallogr. Commun.* **2020**, *76*, 1528−1534.
(32) Simoncic, P.; Romeijn, E.; Hovestreydt, E.; Steinfeld, G.; Santiso-Quiñones, G.; Merkelbach, J. Electron Crystallography and Dedicated Electron-Diffraction Instrumentation. *Struct. Rep.* **2023**, *79* (5), 410−422.
(33) Truong, K.-N.; Ito, S.; Wojciechowski, J. M.; Göb, C. R.; Schürmann, C. J.; Yamano, A.; Del Campo, M.; Okunishi, E.; Aoyama, Y.; Mihira, T.; Hosogi, N.; Benet-Buchholz, J.; Escudero-Adán, E. C.; White, F. J.; Ferrara, J. D.; Bücker, R. Making the Most of 3D Electron Diffraction: Best Practices to Handle a New Tool. *Symmetry* **2023**, *15* (8), 1555.
(34) Andrusenko, I.; Gemmi, M. 3D Electron Diffraction for Structure Determination of Small-Molecule Nanocrystals: A Possible Breakthrough for the Pharmaceutical Industry. *Wiley Interdiscip. Rev.: Nanomed. Nanobiotechnol.* **2022**, *14* (5), No. e1810.
(35) Andrusenko, I.; Hamilton, V.; Mugnaioli, E.; Lanza, A.; Hall, C.; Potticary, J.; Hall, S. R.; Gemmi, M. The Crystal Structure of Orthocetamol Solved by 3D Electron Diffraction. *Angew. Chem., Int. Ed.* **2019**, *58* (32), 10919−10922.
(36) Andrusenko, I.; Hamilton, V.; Lanza, A. E.; Hall, C. L.; Mugnaioli, E.; Potticary, J.; Buanz, A.; Gaisford, S.; Piras, A. M.; Zambito, Y.; Hall, S. R.; Gemmi, M. Structure Determination, Thermal Stability and Dissolution Rate of δ-Indomethacin. *Int. J. Pharm.* **2021**, *608*, No. 121067.
(37) Anyfanti, G.; Husanu, E.; Andrusenko, I.; Marchetti, D. The crystal structure of olanzapine form III. *IUCrJ.* **2024**, *11*.
(38) Kim, L. J.; Ohashi, M.; Zhang, Z.; Tan, D.; Asay, M.; Cascio, D.; Rodriguez, J. A.; Tang, Y.; Nelson, H. M. Prospecting for Natural Products by Genome Mining and Microcrystal Electron Diffraction. *Nat. Chem. Biol.* **2021**, *17* (8), 872−877.
(39) Gurung, K.; Šimek, P.; Jegorov, A., Jr.; Palatinus, L. Structure and Absolute Configuration of Natural Fungal Product Beauveriolide I, Isolated from Cordyceps Javanica, Determined by 3D Electron Diffraction. *Acta Crystallogr., Sect. C: Struct. Chem.* **2024**, *80* (3), 56−61.
(40) Tu, W.; Li, X.; Chen, Z.; Liu, Y. D.; Labardi, M.; Capaccioli, S.; Paluch, M.; Wang, L.-M. Glass formability in medium-sized molecular systems/pharmaceuticals. I. Thermodynamics vs. kinetics. *J. Chem. Phys.* **2016**, *144* (17), 174502.
(41) Ling, Y.; Sun, T.; Guo, L.; Si, X.; Jiang, Y.; Zhang, Q.; Chen, Z.; Terasaki, O.; Ma, Y. Atomic-Level Structural Responsiveness to Environmental Conditions from 3D Electron Diffraction. *Nat. Commun.* **2022**, *13* (1), 6625.
(42) Li, J.; Lin, C.; Ma, T.; Sun, J. Atomic-Resolution Structures from Polycrystalline Covalent Organic Frameworks with Enhanced Cryo-CRED. *Nat. Commun.* **2022**, *13* (1), 4016.
(43) Ouiyangkul, P.; Tantishaiyakul, V.; Hirun, N. Exploring Potential Coformers for Oxyresveratrol Using Principal Component Analysis. *Int. J. Pharm.* **2020**, *587*, No. 119630.
(44) Yamauchi, M.; Lee, E. H.; Otte, A.; Byrn, S. R.; Carvajal, M. T. Contrasting the Surface and Bulk Properties of Anhydrate and Dehydrated Hydrate Materials. *Cryst. Growth Des.* **2011**, *11* (3), 692−698.
(45) Mirza, S.; Miroshnyk, I.; Rantanen, J.; Aaltonen, J.; Harjula, P.; Kiljunen, E.; Heinämäki, J.; Yliruusi, J. Solid-State Properties and Relationship between Anhydrate and Monohydrate of Baclofen. *J. Pharm. Sci.* **2007**, *96* (9), 2399−2408.
(46) Sancho-García, J. C.; Pérez-Jiménez, A. J. A Theoretical Study of the Molecular Structure and Torsional Potential of Styrene. *J. Phys. B: At., Mol. Opt. Phys.* **2002**, *35* (6), 1509−1523.
(47) Bernstein, J.; Davey, R. J.; Henck, J.-O. Concomitant Polymorphs. *Angew. Chem., Int. Ed.* **1999**, *38* (23), 3440−3461.
(48) Gemmi, M.; Lanza, A. E. 3D Electron Diffraction Techniques. *Acta Crystallogr., Sect. B: Struct. Sci., Cryst. Eng. Mater.* **2019**, *75*, 495−504.
(49) Vincent, R.; Midgley, P. A. Double Conical Beam-Rocking System for Measurement of Integrated Electron Diffraction Intensities. *Ultramicroscopy* **1994**, *53* (3), 271−282.
(50) Yang, T.; Xu, H.; Zou, X. Improving Data Quality for Three-Dimensional Electron Diffraction by a Post-Column Energy Filter and a New Crystal Tracking Method. *J. Appl. Crystallogr.* **2022**, *55*, 1583−1591.
(51) Nederlof, I.; Van Genderen, E.; Li, Y.-W.; Abrahams, J. P. A Medipix Quantum Area Detector Allows Rotation Electron Diffraction Data Collection from Submicrometre Three-Dimensional Protein Crystals. *Acta Crystallogr., Sect. D: Biol. Crystallogr.* **2013**, *69* (7), 1223−1230.
(52) Dobro, M. J.; Melanson, L. A.; Jensen, G. J.; McDowall, A. W. *Chapter Three - Plunge Freezing for Electron Cryomicroscopy*, 1st ed.; Elsevier Inc., 2010; Vol. *481*.
(53) Palatinus, L.; Brázda, P.; Jelínek, M.; Hrdá, J.; Steciuk, G.; Klementová, M. Specifics of the Data Processing of Precession Electron Diffraction Tomography Data and Their Implementation in the Program PETS2.0. *Acta Crystallogr., Sect. B: Struct. Sci., Cryst. Eng. Mater.* **2019**, *75*, 512−522.

https://doi.org/10.1021/acsomega.4c05292
ACS Omega 2024, 9, 41555−41564

(54) Burla, M. C.; Caliandro, R.; Carrozzini, B.; Cascarano, G. L.; Cuocci, C.; Giacovazzo, C.; Mallamo, M.; Mazzone, A.; Polidori, G. Crystal Structure Determination and Refinement via SIR2014. *J. Appl. Crystallogr.* **2015**, *48* (1), 306−309.
(55) Sheldrick, G. M. A Short History of SHELX. *Acta Crystallogr., Sect. A: Found. Crystallogr.* **2008**, *64* (1), 112−122.
(56) Petříček, V.; Palatinus, L.; Plášil, J.; Dušek, M. Jana2020 − a New Version of the Crystallographic Computing System Jana. *Z. Kristallogr. - Cryst. Mater.* **2023**, *238* (7−8), 271−282.
(57) Palatinus, L.; Corrêa, C. A.; Steciuk, G.; Jacob, D.; Roussel, P.; Boullay, P.; Klementová, M.; Gemmi, M.; Kopeček, J.; Domeneghetti, M. C.; Cámara, F.; Petříček, V. Structure Refinement Using Precession Electron Diffraction Tomography and Dynamical Diffraction: Tests on Experimental Data. *Acta Crystallogr., Sect. B: Struct. Sci., Cryst. Eng. Mater.* **2015**, *71*, 740−751.
(58) Momma, K.; Izumi, F. VESTA 3 for Three-Dimensional Visualization of Crystal, Volumetric and Morphology Data. *J. Appl. Crystallogr.* **2011**, *44* (6), 1272−1276.
(59) MacRae, C. F.; Sovago, I.; Cottrell, S. J.; Galek, P. T. A.; McCabe, P.; Pidcock, E.; Platings, M.; Shields, G. P.; Stevens, J. S.; Towler, M.; Wood, P. A. Mercury 4.0: From Visualization to Analysis, Design and Prediction. *J. Appl. Crystallogr.* **2020**, *53*, 226−235.
(60) Frisch, M. J.; Trucks, G. W.; Schlegel, H. B.; Scuseria, G. E.; Robb, M. A.; Cheeseman, J. R.; Scalmani, G.; Barone, V.; Petersson, G. A.; Nakatsuji, H.; Li, X.; Caricato, M.; Marenich, A. V.; Bloino, J.; Janesko, B. G.; Gomperts, R.; Mennucci, B.; Hratchian, H. P.; Ortiz, J. V.; Izmaylov, A. F.; Sonnenberg, J. L.; Williams-Young, D.; Ding, F.; Lipparini, F.; Egidi, F.; Goings, J.; Peng, B.; Petrone, A.; Henderson, T.; Ranasinghe, D.; Zakrzewski, V. G.; Gao, J.; Rega, N.; Zheng, G.; Liang, W.; Hada, M.; Ehara, M.; Toyota, K.; Fukuda, R.; Hasegawa, J.; Ishida, M.; Nakajima, T.; Honda, Y.; Kitao, O.; Nakai, H.; Vreven, T.; Throssell, K.; Montgomery, J. A.; Peralta, Jr., J. E.; Ogliaro, F.; Bearpark, M. J.; Heyd, J. J.; Brothers, E. N.; Kudin, K. N.; Staroverov, V. N.; Keith, T. A.; Kobayashi, R.; Normand, J.; Raghavachari, K.; Rendell, A. P.; Burant, J. C.; Iyengar, S. S.; Tomasi, J.; Cossi, M.; Millam, J. M.; Klene, M.; Adamo, C.; Cammi, R.; Ochterski, J. W.; Martin, R. L.; Morokuma, K.; Farkas, O.; Foresman, J. B.; Fox, D. J. Gaussian. Inc.: Wallingford CT.

https://doi.org/10.1021/acsomega.4c05292
ACS Omega 2024, 9, 41555−41564